Accepted Manuscript

Copper-silicon dioxide nanocomposites: Structure and electron transport

Ivan A. Svito, Olga V. Korolik, Alexander V. Mazanik, Alexander K. Fedotov, Anis M. Saad, Valery G. Luhin, Tomasz N. Koltunowicz, Pawel Zukowski

PII: S0925-8388(17)32692-0

DOI: 10.1016/j.jallcom.2017.07.310

Reference: JALCOM 42726

To appear in: *Journal of Alloys and Compounds*

Received Date: 13 April 2017

Revised Date: 20 July 2017

Accepted Date: 28 July 2017

Please cite this article as: I.A. Svito, O.V. Korolik, A.V. Mazanik, A.K. Fedotov, A.M. Saad, V.G. Luhin, T.N. Koltunowicz, P. Zukowski, Copper-silicon dioxide nanocomposites: Structure and electron transport, *Journal of Alloys and Compounds* (2017), doi: 10.1016/j.jallcom.2017.07.310.

Copper-silicon dioxide nanocomposites: structure and electron transport

Ivan A. Svito[1], Olga V. Korolik[1], Alexander V. Mazanik[1], Alexander K. Fedotov[1], Anis M. Saad[2], Valery G. Luhin[3], Tomasz N. Koltunowicz[4], Pawel Zukowski[4,*]

[1] Belarusian State University, 4 Nezalezhnastsi Av., 220030 Minsk, Belarus

[2] Al Balqa Applied University, Physics Department, PO Box 4545, 11953 Amman, Jordan

[3] Belarusian State Technological University, Center of Physical and Chemical Investigation Methods, 13A Sverdlova Str., Minsk, Belarus

[4] Lublin University of Technology, 38D Nadbystrzycka Str., 20-618 Lublin, Poland

Abstract

We investigated correlation between structure and electron transport properties of composite films synthesized by the ion-beam sputtering of Cu + SiO_2 target. Photoluminescence (PL) spectra testify to an oxygen deficiency in the silicon dioxide matrix in agreement with the Raman spectroscopy, which reveals the presence of Cu_2O phase along with elemental copper. For the nanocomposites with copper atomic fraction $x < 0.64$, the temperature dependence of conductivity obeys $\ln(\sigma) \sim T^{-0.5}$ law at low temperatures (electron tunneling between size distributed copper nanoparticles) replacing with the Mott Variable Range Hopping (VRH) with the temperature increase. Electron transport properties of the studied nanocomposites are significantly affected by matrix defectiveness, which increases with metallic phase content according to PL study. The increasing matrix defectiveness results in decrease of crossover temperature from tunneling to VRH conductivity, as well as growth of matrix permittivity due to an enhanced contribution of electrons localized at defects.

[*] Corresponding author. Tel: +48 81 5384713. E-mail: t.koltunowicz@pollub.pl (Tomasz N. Koltunowicz)

Keywords: Nanocomposite, Copper, Silicon dioxide, Defects, Permittivity, Electron transport.

1. Introduction

Nanostructured metal-dielectric nanocomposite materials have attracted a great interest due to their unusual optical [1-3] and electrophysical [4] properties. In particular, they provide a possibility to tune optical response and electrical resistivity on a broad scale; nonmagnetic $Cu_x(SiO_2)_{1-x}$ nanocomposites reveal a giant Hall effect [5]. Such nanocomposites possess a high corrosion hardness and stability [6, 7]; high degree of their defectiveness and amorphous state of matrix provide them an excellent radiation hardness [8]. Possibility to prepare nanocomposites with "core-shell" structure (copper core surrounded by Cu_2O shell) is promising for catalytic applications [9-13]. Since copper nanoparticles display the localized plasmon resonance in the visible spectral range, the photocatalytic activity of such materials can be improved due to the well-known phenomenon of local light intensity enhancement [14, 15].

Understanding the structure and electron transport mechanisms in the nanocomposites is a prerequisite to control their properties. It was demonstrated in our previous work [16] that the copper is distributed in form of nanoparticles, and there is an additional Cu_2O phase along with copper and silicon oxide. However, no correlation between structure of nanocomposites and their electron transport properties were established so far, which predetermined the purpose of the present work.

2. Experimental section

Nanocomposites were synthesized by the ion-beam sputtering of the two-component target ($Cu+SiO_2$) on a water-cooled glass ceramic substrate (240×60 mm^2, resistivity of 10^{16} Ω·cm) in the argon atmosphere with partial pressure $p_{Ar}=9.6\cdot10^{-2}$ Pa. Both substrate and target were

subjected to argon plasma cleaning for 30 min before deposition process. During synthesis, ion beam current density and accelerating voltage were held equal to 0.9 mA/cm^2 and 3.5 kV, respectively. The used target represented 270×70 mm^2 copper plate with thin SiO_2 strips (80×10×1 mm^3) placed on top of it. Irregular placing of SiO_2 strips enabled one to obtain the deposit with composition varying along the long side of the substrate. Cutting of the substrate with deposited film normally to the gradient of Cu concentration *x* allowed to get a large series of samples with different compositions and prepared in a single technological cycle.

The synthesis procedure was described in more details in previous works [16, 17]. According to the energy-dispersive X-ray analysis and cross-sectional scanning electron microscopy, the atomic fraction of metallic phase *x* in the studied composites varied from 0.39 to 0.71, and the film thickness – from 1.2 to 2.7 μm.

X-ray diffraction (XRD) analysis was done using a Bruker D8 Advance diffractometer (Bragg-Brentano geometry, Cu K_α emission). Specular reflectance spectra were taken with a MC122 spectrometer (Proscan Special Instruments, Belarus) with spectral resolution about 3 nm. Raman and photoluminescence (PL) spectra were measured using a Nanofinder HE confocal spectrometer (Lotis TII, Belarus-Japan) with spectral resolution about 3 cm^{-1} (0.1 nm). Solid-state lasers (emission wavelength of 355, 473 or 532 nm) were used as excitation sources; signal was detected with a cooled CCD-matrix with acquisition time typically equal to 120 s. Spectral calibration was done using a built-in gas-discharge lamp providing accuracy about 3 cm^{-1} (0.1 nm). All Raman and PL spectra were measured on the freshly polished samples.

For electric measurements, rectangular 2×10 mm^2 samples provided by the ultrasonically soldered indium contacts were used. The distance between potential probes was determined using stage micrometer with an accuracy of 0.005 mm and was equal to 7±0.1 mm. Temperature dependences of DC conductivity were studied in the range from 2 to 300 K with a HFMS system (Cryogenic Limited, London; accuracy of sample temperature setting better than 0.05 K). DC conductivity was measured using four-probe method with Keithley 6430 source-meter and

Keithley 2182A nanovoltmeter. Agilent E4980A and an Agilent E4285A LCR-meters were used for measurements of AC conductivity (room temperature, frequency range from 100 Hz to 30 MHz, probe voltage magnitude of 40 mV, standard correction procedure). AC conductivity was measured using two-probe method. Correction of the open circuit voltage mode was done with a clean glass ceramic substrate provided by contacts placed in the same geometry as for the nanocomposite samples.

3. Results and Discussion

3.1. Structural characterization

XRD patterns of the synthesized composites demonstrate three characteristic peaks (Fig. 1) at $2\theta = 43.35°$, 50.30° and 74.11° corresponding to diffraction from the (111), (200) and (220) planes of elemental copper with face-centered cubic lattice (JCPDS No. 04-0836). A low-intensity wide signal in the range of $15 \leq 2\theta \leq 25°$ can be related to amorphous matrix [18]. The Scherrer equation reveals a gradual increase of granules' size from 5 to 9 nm with increasing content of metallic phase *x* from 0.39 to 0.71.

Specular reflection spectra of the nanocomposites demonstrate a pronounced feature at 1.9–2.2 eV (Fig. 2a). However, the shape of spectra in this range strongly depends on *x*. Spectra of the composites with a high content of metallic phase are similar to that for the reference Cu foil and demonstrate a step related to electron transitions from *d*- to *s*-band [19, 20]. On the contrary, for the composites with a relative low content of copper, a distinct peak is observed instead the step. This peak can be related to light scattering due to resonant excitation of surface plasmons in the copper nanoparticles [3, 21, 22].

As is known [19], for a single particle embedded in a non-conducting medium with permittivity ε_m, the excitation of surface plasmons corresponds to minimum of the frequency dependent function

$$f(\omega) = [\varepsilon_1(\omega) + \varepsilon_m]^2 + [\varepsilon_2(\omega)]^2, \quad (1)$$

where $\varepsilon_1(\omega)$ and $\varepsilon_2(\omega)$ are the real and imaginary parts of nanoparticle dielectric function $\varepsilon(\omega)=\varepsilon_1(\omega)+i\varepsilon_2(\omega)$. Since the average size of copper nanoparticles in the studied nanocomposites is much less as compared to mean free path l of electrons in bulk copper, (l=42 nm, [22]), one should modify dielectric function of bulk copper to take into account additional electron scattering at surface. Within the framework of the Kreibig model [22], $\varepsilon(\omega)$ can be presented for nanoparticle as

$$\varepsilon(\omega) = \varepsilon_{bulk}(\omega) + \omega_p^2\left(\frac{1}{\omega^2+\Gamma_0^2} - \frac{1}{\omega^2+\Gamma(R)^2}\right) + i\frac{\omega_p^2}{\omega}\left(\frac{\Gamma(R)}{\omega^2+\Gamma(R)^2} - \frac{\Gamma_0}{\omega^2+\Gamma_0^2}\right), \quad (2)$$

where $\varepsilon_{bulk}(\omega)$ is the dielectric function of bulk copper, ω_p is the plasma frequency in copper ($\omega_p = 1.4\cdot10^{16}$ s^{-1}, [21]), $\Gamma_0 = v_F/l$ is the electron damping constant in bulk copper, v_F is the Fermi velocity ($v_F=1.57\cdot10^6$ m/s, [22]), and the size-dependent damping constant is determined as

$$\Gamma(R) = \Gamma_0 + \frac{Av_F}{R}, \quad (3)$$

where R is the size of nanoparticles, and A is the dimensionless parameter, which depends on the scattering mechanism at the surface. Figure 2b presents $f(\omega)$ function calculated according to Eqs. (1) – (3) using $\varepsilon_{bulk}(\omega)$ function taken from [23], R = 5 nm, A = 1, and with different values of matrix permittivity ε_m. One can see that for ε_m = 3.7 (permittivity of SiO_2), function $f(\omega)$ has minimum at 2.25 eV, which differs substantially from position of maxima in the reflectance spectra, whereas for higher values of ε_m a good agreement with experiment takes place. This fact indicates that copper nanoparticles are surrounded by a medium different from silicon dioxide. The observed slight red shift in position of surface plasmon resonance (SPR) with increased x can be related to electrodynamic coupling of closely packed nanoparticles [24].

Room temperature Raman spectra of the nanocomposites and reference electrodeposited Cu_2O film are presented in Fig. 3. One can see peaks at 215, 425, 500, 520 and 642 cm^{-1}. According to [25], the peaks at 215, 425, 500, and 642 cm^{-1} correspond to scattering on optical phonons in Cu_2O indicating formation of this phase in the composites. Intensity of these peaks increases with *x*. Their large spectral width (FWHM≈25 cm^{-1} for peak at 215 cm^{-1}) and rather low intensity point to a high disorder degree of Cu_2O phase correlating with absence of reflexes corresponding to Cu_2O in XRD patterns (Fig. 1). For the composite with the highest Cu content ($x = 0.70$) signal in the range of Raman shifts from 480 to 540 cm^{-1} is clearly split into two peaks with maxima at 497 and 520 cm^{-1}. The first one belongs to Cu_2O, whereas the second one can be attributed to elemental Si [26]. Taking into account a high inclination of copper to oxidation, it is reasonably to presume that copper nanoparticles in the studied composites are surrounded by oxide shells formed primary by Cu_2O phase. Note that substitution of Cu_2O permittivity ($\varepsilon_{Cu_2O} = 7.5$ [27]) to Eq. (1) gives a good agreement between calculated spectral position of SPR (2.05 eV, Fig. 2b) and maxima in reflection spectra (Fig. 2a). The appearance of peak corresponding to elemental silicon indicates depletion of oxide matrix by oxygen, which correlates with the revealed oxidation of copper.

Fig. 4 demonstrates a relative broad band (with full width at half-maximum of appr. 0.3 eV), which may be associated with photoluminescence in the studied composites. In the case of excitation at 473 or 532 nm, this peak is red shifting by a few tens of meV with increasing content of metallic phase. At the same time, this shift disappears, if more short-wave radiation (355 nm) is used for PL excitation. On the first glance, PL shift could be related to presence of the Cu_2O phase in the nanocomposites because a typical size of Cu_2O particles cannot exceed a few nanometers and they should reveal the well-known electron quantum confinement effect [19]. However, the spectral position and shape of the observed PL band do not correspond to the known data for Cu_2O [28] indicating that photoluminescence is related to the copper nanoparticles. Since their size exceeds substantially the de Broglie wavelength of electron,

quantum confinement effect cannot affect the electron spectrum in copper nanoparticles and, hence, the size-dependent photoluminescence has another origin. We believe that the observed PL arises from recombination of electrons excited to *s*-band with the holes in *d*-band. Since spectral position of the observed PL band is close to position of SPR, there is a wavelength-dependent absorption of PL radiation by copper nanoparticles, which gives rise to the observed shift of PL maximum. In the case of a short-wavelength excitation, PL signal is generated in a thinner near-surface layer (due to an increased absorption), and effect of interaction of emitted light with nanoparticles becomes less pronounced.

Low temperature (23 K) PL spectra with UV excitation (355 nm) were measured for investigation of defects in the dielectric matrix (Fig. 5).

As seen from Fig. 5, PL spectra can be fitted well by a superposition of six Gauss lines peaked at 1.9, 2.1, 2.4, 2.6, 2.8, and 3.1 eV. Band at 2.1 eV is related to Cu nanoparticles, as it was mentioned above. The peak at 1.9 eV is attributed to single-coordinated oxygen atoms [29-31], and the peak at 3.1 eV – to neutral oxygen divacancy (silylene center) [29, 32, 33]. The peaks at 2.4–2.8 eV are originated from the neutral oxygen monovacancies with Si-Si bond [29, 33-35]. Dispersion in the distance between silicon atoms in such defects explains the scattering in energy of electron transitions from 2.4 to 2.8 eV [35]. As is seen, an increase of metallic phase content leads to growth in relative intensity of 2.4–2.8 and 3.1 eV bands (Fig. 5). This fact points to progressive influence of copper oxidation on the structure of nanocomposites, which results in rising oxygen deficiency in the silicon oxide matrix.

Thus, the real phase composition of the nanocomposites is more complicated as compared to that of the target, and the used notation "$Cu_x(SiO_2)_{1-x}$" should be considered only as simplified.

3.2. Electron transport

The mechanisms of electron transport in composite materials are known to be substantially dependent on the ratio and structural state of metallic and dielectric phases, which, in turn, are determined by the synthesis atmosphere, target composition and temperature and other factors. In particular, when the intergranular distance becomes less than the electron localization length or when the concentration of matrix defects N_{def} satisfies the Mott criterion $N_{def}^{1/3}\alpha_B \approx 0.25$ (α_B is the Bohr radius of electron localized at defect), metal-insulator transition (MIT) takes place due to formation of conductive net [36]. This results in separation of nanocomposites into "dielectric-like" and "metallic-like", which manifests itself both in different types of their DC conductivity temperature dependences (Fig. 6) and character of impedance (capacitive-like or inductive-like, Fig. 7).

As seen from Fig. 6, the nanocomposites with atomic fraction of copper $x > 0.68$ possess a positive temperature coefficient of resistance $d\rho/dT$ in the temperature range 25 K < T < 300 K. For the samples with $x < 0.64$, $d\rho/dT$ is negative in the whole temperature range, i.e. an activation-like temperature dependence of resistance is dominating (Fig. 6). For the range $0.61 < x < 0.64$, a trend to linearization in the $\sigma \sim \ln(T)$ coordinates is observed, which can be determined by a tunnel electron transport with a high localization length near the MIT [37, 38]; some deviation from $\sigma \sim \ln(T)$ dependence is believed due to agglomeration of granules in the composites and formation of prolonged chains with metallic conductivity.

Figure 6 shows that there is a certain ambiguity in determination of the percolation threshold x_c from $\sigma(T)$ dependences. As it was demonstrated in our previous work for the $(FeCoZr)_x(Al_2O_3)_{1-x}$ nanocomposites [39], x_c can be found from analysis of impedance of the nanocomposites. Indeed, since each conductor possesses an inductivity, impedance of the composites with $x \geq x_c$ is of inductive-like type due to formation of continuous conductive cluster between two contacts. On the contrary, if $x < x_c$, impedance is capacitive-like due to separation of metallic particles by oxide interlayers [40, 41].

As seen from Fig. 7a, when the atomic fraction of copper reaches $x_c \approx 0.64$, impedance changes from capacitive-like to inductive-like pointing to formation of the infinite conductive cluster. So, the indicated value $x_c \approx 0.64$ can be associated with the metal-insulator transition.

DC conductivity for the nanocomposites with $x < x_c$ reveals activation-like temperature dependence, at that the activation energy increases with temperature. These dependences were analyzed both using linearization in the $\ln(\sigma) \sim T^{-n}$ coordinates (Figs. 8a–c) and the Zabrodski method [42] based on consideration of reduced activation energy. Both these approaches have demonstrated that there is a crossover temperature 30 K< $T_c(x)$ < 130 K for the $Cu_x(SiO_2)_{1-x}$ nanocomposites with $x \leq x_c \approx 0.64$ (Fig. 8d). In the $\ln(\sigma) \sim T^{-n}$ dependences, $n = 0.5$ for $T < T_c$ and $n = 0.25$ for $T > T_c$ (Fig. 8).

The $\ln(\sigma) \sim (T_{01}/T)^{0.25}$ law is known to be inherent to the Mott variable range hopping [43], whereas the $\ln(\sigma) \sim (T_{02}/T)^{0.5}$ conductivity dependence is usually explained as a consequence of a Coulomb gap in the energy distribution of the localized electronic states (the Shklovski–Efros law, [44]). However, the Shklovski–Efros conductivity mechanism can be realized only at low temperatures (as a rule, less than 10 K). Since in our case the $\ln(\sigma) \sim (T_{02}/T)^{0.5}$ law is observed at much higher temperatures (up to 120 K), another explanation is required. Like in our previous work [39], we have attracted the model proposed in [45] for description of electron transport at $T < T_c$. In the framework of this model, conductivity in granular media is realized by thermally activated electron tunneling between neighboring granules, which have some scattering of their size. According to the previous studies [46, 47], the scattering of granules size can reach 30 % in the nanocomposites produced by the ion-beam sputtering. The parameter T_{02}, which characterizes the activation energy, is determined as [45]:

$$T_{02} = \frac{q_e^2}{k_B \varepsilon a_0} \cdot \left(\frac{a_0}{\lambda}\right)^{3/2} \cdot \left[x_v^{-1/2} \cdot \left(1 - \frac{x_v}{x_{vc}}\right)^{1/3}\right]. \qquad (4)$$

Here q_e is the electron charge, k_B is the Boltzmann constant, ε is the matrix permittivity, a_0 is the average size of granules, λ is the electron localization length, x_v is the volume fraction of metallic

phase in the nanocomposite, and x_{vc} is the volume fraction corresponding to the metal-insulator transition.

Eq. (4) enables one to calculate dependence of static matrix permittivity ε on content of metallic phase in the nanocomposites (Fig. 9). In our calculations, the parameter a_0 has been set as increasing from 5 to 9 nm with increase of x from 0.44 to 0.62 according to XRD data; x_{vc} has been determined from impedance analysis (Fig. 7), and $\lambda = h/\sqrt{2m^* U_{ab}}$ has been estimated using electron effective tunneling mass $m^* = 0.41\ m_0$ [48] and the height of intergranular barrier U_{ab} = 3.7 eV (difference between Cu work function and silicon oxide electron affinity). It is seen that the permittivity increases approximately by one order of magnitude when x is increasing from 0.39 to 0.63 and exceeds significantly permittivity of both SiO_2 and Cu_2O (Fig. 9). High values of matrix permittivity can be related to its defectiveness, which gives rise to significant contribution of electrons localized on defects to screening of electric field. Such behavior is typical for highly-doped semiconductors and was reported by many authors [49-51].

The increase of permittivity with x correlates well with the PL data discussed above. Indeed, the increase of copper content (which acts as reducer of SiO_2) gives rise to increase of oxygen deficient defects in silicon oxide matrix (Fig. 5). One can suppose that these defects contribute to screening of electric field providing the growth of permittivity with x. Progressive increase in concentration of matrix defects makes more favorable the Mott variable hopping conductivity, which results in decrease of crossover temperature T_c with x.

Conclusions

Ion-beam sputtering of two-component Cu+SiO_2 target leads to formation of nanostructured composites, in which Cu_2O phase exists along with copper nanoparticles. Copper oxidation results in oxygen deficiency in silicon oxide matrix, which manifests itself in photoluminescence spectra. For the nanocomposites on the dielectric side of metal-insulator transition, electrical conductivity increases with temperature according to $\ln(\sigma) \sim T^{-n}$ law, where

n equals to 0.5 and 0.25 at low and high temperatures, respectively. The $\ln(\sigma) \sim T^{-0.5}$ law is attributed to electron tunneling between granules having some scattering of size, whereas $\ln(\sigma) \sim T^{-0.25}$ law is related to the Mott variable range hopping. Increase of copper content in the nanocomposites is accompanied by increased concentration of defects in silicon oxide matrix, which is manifested in increase of its permittivity and decrease in temperature of crossover from tunneling to VRH electron transport.

Acknowledgements

The authors also acknowledge stimulating discussions with A.N. Ponyavina, E.A. Streltsov, and A.D. Zamkovets.

The work was partly supported by the Research Programs "Photonics, Opto- and Microelectronics" (contract No 1.2.02) of the Republic of Belarus and by the statute tasks of the Lublin University of Technology, at the Faculty of Electrical Engineering and Computer Science, 8620/E-361/S/2016 (S-28/E/2016), entitled "*Researches of electrical, magnetic, thermal and mechanical properties of modern electrotechnical and electronic materials, including nanomaterials and electrical devices and their components, in order to determination of suitability for use in electrical engineering and to increase the efficiency of energy management*".

References

[1] G.A. Niklasson, C.G. Granqvist, Optical properties and solar selectivity of co-evaporated Co-Al_2O_3 composite films, J. Appl. Phys. 55 (1984) 3382–3410.

[2] O.A. Aktsiperov, P.V. Elyutin, A.A. Nikulin, E.A. Ostrovskaya, Size effects in optical second-harmonic generation by metallic nanocrystals and semiconductor quantum dots: The role of quantum chaotic dynamics, Phys. Rev. B 51 (1995) 17591.

[3] O.A. Yeshchenko, I.M. Dmitruk, A.M. Dmytruk, A.A. Alexeenko, Influence of annealing conditions on size and optical properties of copper nanoparticles embedded in silica matrix, Mat. Sci. Eng. B 137 (2007) 247–254.

[4] B. Abeles, P. Sheng, M.D. Coutts, Y. Arie, Structural and electrical properties of granular metal films, Adv. Phys. 24 (1975) 407–461.

[5] X.X. Zhang, C. Wan, H. Liu, Z.Q. Li, P. Sheng, J. J. Lin, Giant Hall effect in nonmagnetic granular metal films, Phys. Rev. Lett. 86 (2001) 5562.

[6] A.D. Pogrebnjak, I.V. Yakushchenko, O.V. Bondar, V.M. Beresnev, K. Oyoshi, O.M. Ivasishin, H. Amekura, Y. Takeda, M. Opielak, C. Kozak, Irradiation resistance, microstructure and mechanical properties of nanostructured (TiZrHfVNbTa)N coatings, J. All. Comp. 679 (2016) 155–163.

[7] A.V. Pshyk, L.E. Coy, G. Nowaczyk, M. Kempiński, B. Peplińska, A.D. Pogrebnjak, V.M. Beresnev, S. Jurga, High temperature behavior of functional TiAlBSiN nanocomposite coatings, Surf. Coat. Tech. 305 (2016) 49–61.

[8] Kusi-Shu, Chang Jiao, Jenu-Gwo, Improvement of hot-carrier and radiation hardnesses in metal-oxide-nitride-oxide semiconductor devices by irradiation-then-anneal treatments, IEEE Trans. ED 41 (1994) 612–614.

[9] Z. Ai, L. Zhang, S. Lee, W. Ho, Interfacial hydrothermal synthesis of Cu@Cu_2O core-shell microspheres with enhanced visible-light-driven photocatalytic activity, J. Phys. Chem. C 113 (2009) 20896–20902.

[10] H. Chen, T. Tu, M. Wen, Q. Wu, Assembly synthesis of Cu_2O-on-Cu nanowires with visible-light-enhanced photocatalytic activity, Dalton Trans. 44 (2015) 15645−15652.

[11] X. Zou, H. Fan, Y. Tian, M. Zhang, X. Yan, Microwave-assisted hydrothermal synthesis of Cu/Cu_2O hollow spheres with enhanced photocatalytic and gas sensing activities at room temperature, Dalton Trans. 44 (2015) 7811−7821.

[12] Z. Jin, Z. Hu, J.C. Yu, J. Wang, Room temperature synthesis of highly active Cu/Cu_2O photocathode for photoelectrochemical water splitting, J. Mater. Chem. A 4 (2016) 13736−13741.

[13] P. Zhang, T. Wang, H. Zeng, Design of Cu-Cu_2O/g-C_3N_4 nanocomponent photocatalysts for hydrogen evolution under visible light irradiation using water-soluble Erythrosin B dye sensitization, Appl. Surf. Sci. 391 (2017) 404–414.

[14] J. Li, S.K. Cushing, J. Bright, F. Meng, T.R. Senty, P. Zheng, A.D. Bristow, N. Wu, Ag@Cu_2O core-shell nanoparticles as visible-light plasmonic photocatalysts, ACS Catal. 3 (2013) 47−51.

[15] D.V. Guzatov, S.V. Vaschenko, V.V. Stankevich, A.Ya. Lunevich, Y.F. Glukhov, S.V. Gaponenko, Plasmonic enhancement of molecular fluorescence near silver nanoparticles: theory, modeling, and experiment, J. Phys. Chem. C 116 (2012) 10723−10733.

[16] I.A. Svito, A.K. Fedotov, T.N. Koltunowicz, P. Zukowski, Y. Kalinin, A. Sitnikov, K. Czarnacka, A. Saad, Hopping of electron transport in granular $Cu_x(SiO_2)_{1-x}$ nanocomposite films deposited by ion-beam sputtering, J. All. Comp. 615 (2014) S371–S374.

[17] O.V. Stognei, Yu.E. Kalinin, A.V. Sitnikov, I.V. Zolotukhin, A.V. Slyusarev, Resistive and magnetoresistive properties of granular amorphous CoFeB-SiO_n composites, Phys. Met. Metallogr. 91 (2001) 21–28.

[18] Z.N. Siddiqui, T. Khan, P_2O_5/SiO_2 as an efficient heterogeneous catalyst for the synthesis of heterocyclic alkene derivatives under thermal solvent-free conditions, Catal. Sci. Technol. 3 (2013) 2032–2043.

[19] S.V. Gaponenko, Introduction to Nanophotonics. Cambridge University Press, Cambridge, 2010.

[20] N.W. Ashcroft, N.D. Mermin. Solid State Physics, Saunders College Publishing, Orlando, 1976.

[21] G.H. Chan, J. Zhao, E.M. Hicks, G.C. Schatz, R.P. Van Duyne, Plasmonic properties of copper nanoparticles fabricated by nanosphere lithography, Nano Lett. 7 (2007) 1947–1952.

[22] U. Kreibig, M. Vollmer. Optical Properties of Metal Clusters. Springer, Berlin, 1995.

[23] H. Ehrenreich, H.R. Philipp, Optical properties of Ag and Cu, Phys. Rev. 28 (1962) 1622–1629.

[24] S.M. Kachan, A.N. Ponyavina, Spectral properties of close-packed monolayers consisted of silver nanospheres, J. Phys.: Cond. Matter. 14 (2002) 103–111.

[25] P.F. Williams, S.P.S. Porto, Symmetry-forbidden resonant Raman scattering in Cu_2O, Phys. Rev. B 8 (1973) 1782–1785.

[26] J.P. Russel, Raman scattering in silicon, Appl. Phys. Lett. 6 (1965) 223–224.

[27] F. Pei, S. Wu, G. Wang, M. Xu, S.Y. Wang, L.Y. Chen, Y. Jia, Electronic and optical properties of noble metal oxides M_2O (M= Cu, Ag and Au): First-principles study, J. Korean Phys. Soc. 55 (2009) 1243.

[28] J. Li, Z. Mei, D. Ye, H. Liang, L. Liu, Y. Liu, A. Galeckas, A.Yu. Kuznetsov, X. Du, Engineering of optically defect free Cu_2O enabling exciton luminescence at room temperature, Opt. Mater. Express 3 (2013) 2072–2077.

[29] L. Skuja, Optically active oxygen-deficiency-related centers in amorphous silicon dioxide, J. Non-Cryst. Sol. 239 (1998) 16–48.

[30] L. Skuja, Isoelectronic series of twofold coordinated Si, Ge, and Sn atoms in glassy SiO_2: a luminescence study, J. Non-Cryst. Sol. 149 (1992) 77–95.

[31] V.B. Sulimov, V.O. Sokolov, Cluster modeling of the neutral oxygen vacancy in pure silicon dioxide, J. Non-Cryst. Sol. 191 (1995) 260–280.

[32] L.N. Skuja, A.N. Streletsky, A.B. Pakovich, A new intrinsic defect in amorphous SiO_2: twofold coordinated silicon, Solid State Comm. 50 (1984) 1069–1072.

[33] V.S. Kortov, A.F. Zatsepin, S.V. Gorbunov, A.M. Murzakaev, Luminescent defects in nanostructured silica, Phys. Solid State 48 (2006) 1273–1279.

[34] V.A. Gritsenko, K.S. Zhuravlev, V.A. Nadolinnyi, Quantization of the electronic spectrum and localization of electrons and holes in silicon quantum dots, Phys. Solid State 53 (2011) 860–863.

[35] J.Y. Zhang, X.M. Bao, N.S. Li, H.Z. Song, Photoluminescence study of defects in Si ion implanted thermal SiO_2 films, J. Appl. Phys. 83 (1998) 3609–3613.

[36] A.G. Zabrodskii, The Coulomb gap: the view of an experimenter, Phil. Mag. B 81 (2001) 1131–1151.

[37] I.S. Beloborodov, K.B. Efetov, A.V. Lopatin, V.M. Vinokur, Transport properties of granular metals at low temperatures. Phys. Rev. Lett. 91 (2003) 246801.

[38] I.S. Beloborodov, A.V. Lopatin, V.M. Vinokur, K.B. Efetov, Granular electronic systems, Rev. Mod. Phys. 79 (2007) 469.

[39] I.A. Svito, A.K. Fedotov, A. Saad, P. Zukowski, T.N. Koltunowicz, Influence of oxide matrix on electron transport in $(FeCoZr)_x(Al_2O_3)_{1-x}$ nanocomposite films, J. All. Comp. 699 (2017) 818–823.

[40] H. Bakkali, M. Dominguez, X. Batlle, A. Labarta, Universality of the electrical transport in granular metals, Sci. Rep. 6, Article number: 29676 (2016).

[41] F.C. Fonseca, R. Muccillo, Impedance spectroscopy analysis of percolation in (yttria-stabilized zirconia)-yttria ceramic composites, Solid State Ionics 166 (2004) 157–165.

[42] A.G. Zabrodski, Sov. Solid State Phys. 11 (1977) 595.

[43] N.F. Mott, E.A. Devis, Electron Processes in Noncrystalline Materials, Clarendon Press, Oxford, 1979.

[44] A.L. Efros, B.I. Shklovski, Conduction of nanostructured metall – insulator, Phys. Stat. Solid. B 76 (1976) 475–490.

[45] E.Z. Meilikhov, Thermally activated conductivity and current-voltage characteristic of dielectric phase in granular metals, J. Exp. Theor. Phys. 88 (1999) 819–825.

[46] K. Yakushiji, S. Mitani, K. Takanashi, Composition dependence of particle size distribution and giant magnetoresistance in Co-Al-O granular films, J. Magn. Magn. Mater. 212 (2000) 75–81.

[47] M. Ohnuma, K. Hono, H. Onodera, Distribution of Co particles in Co-Al-O granular thin films, Journal of Metastable and Nanocrystalline Materials 1 (1999) 171–176.

[48] B. Brar, G.D. Wilk, A.C. Seabaugh, Direct extraction of the electron tunneling effective mass in ultrathin SiO_2, Appl. Phys. Lett. 69 (1996) 2728.

[49] N.A. Poklonski, S.A. Vyrko, A.G. Zabrodskii, Electrostatic models of insulator-metal and metal-insulator concentration phase transitions in Ge and Si crystals doped by hydrogen-like impurities, Phys. Solid State 46 (2004) 1101–1106.

[50] M. Lee, J.G. Massey, V.L. Nguyen, B.I. Shklovskii, Coulomb gap in a doped semiconductor near the metal-insulator transition: Tunneling experiment and scaling ansatz, Phys. Rev. B 60 (1999) 1582.

[51] T.G. Castner, N.K. Lee, H.S. Tan, L. Moberly, O. Symko, The low-frequency, low-temperature dielectric behavior of *n*-type germanium below the insulator-metal transition, J. Low Temp. Phys. 38 (1980) 447–473.

Figure captions

Fig. 1. XRD patterns of $Cu_x(SiO_2)_{1-x}$ nanocomposites.

Fig. 2. Specular reflection spectra of $Cu_x(SiO_2)_{1-x}$ nanocomposites and reference Cu foil (*a*); function $f(\omega)=[\varepsilon_1(\omega)+\varepsilon_m]^2 + [\varepsilon_2(\omega)]^2$ (Eq. (1)) calculated for different values of matrix permittivity ε_m (*b*).

Fig. 3. Raman spectra of $Cu_x(SiO_2)_{1-x}$ nanocomposites (*a*) and reference Cu_2O film (*b*). Excitation: 473 nm / 0.6 mW (*a*) and 473 nm / 25 μW (*b*).

Fig. 4. PL spectra of $Cu_x(SiO_2)_{1-x}$ nanocomposites. Excitation: 473 nm / 80 μW.

Fig. 5. PL spectra taken at 23 K under 355 nm / 4 mW excitation and their fitting by Gauss lines for $Cu_x(SiO_2)_{1-x}$ nanocomposites with x=0.40 (*a*) and x=0.71 (*b*).

Fig. 6. Temperature dependences of conductivity normalized to the room temperature σ/σ_{300K} for the $Cu_x(SiO_2)_{1-x}$ nanocomposites with different content of metallic phase.

Fig. 7. Frequency (*a*) and concentration (*b*) dependences of the phase shift Θ between AC voltage and current for the $Cu_x(SiO_2)_{1-x}$ nanocomposites.

Fig. 8. Temperature dependences of electrical conductivity of the $Cu_x(SiO_2)_{1-x}$ nanocomposites in different coordinates (*a*) - (*c*); crossover temperature T_c depending on metallic phase fraction (*d*).

Fig. 9. Matrix permittivity ε for $Cu_x(SiO_2)_{1-x}$ nanocomposites calculated using Eq. (4).

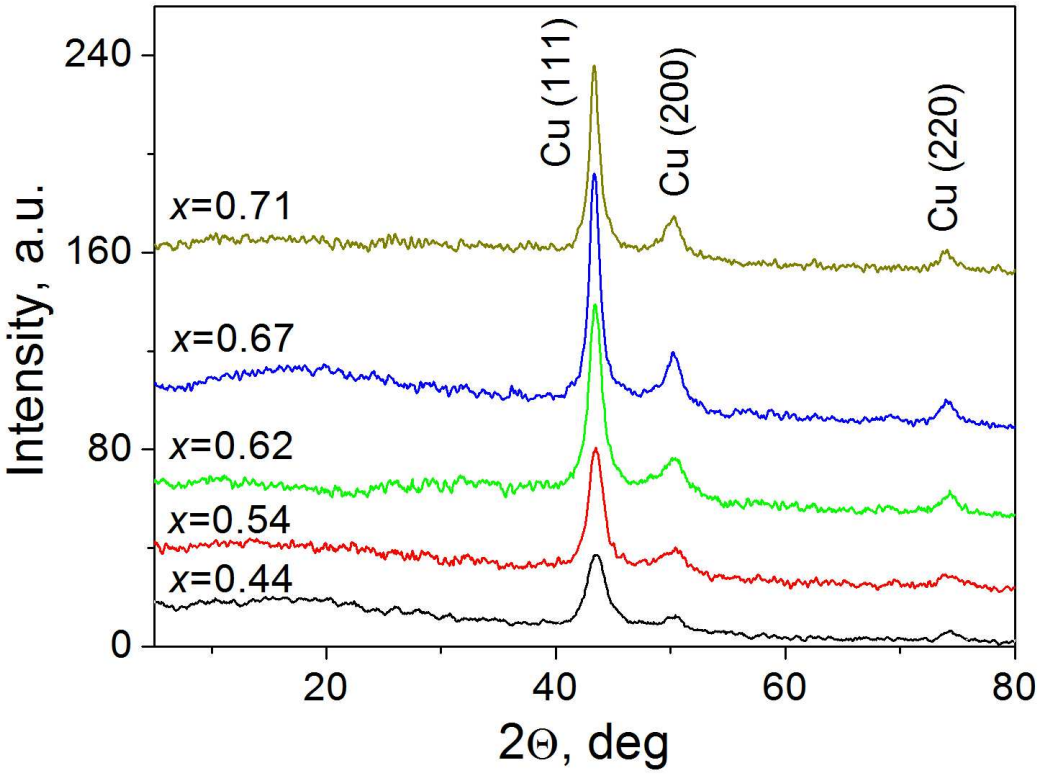

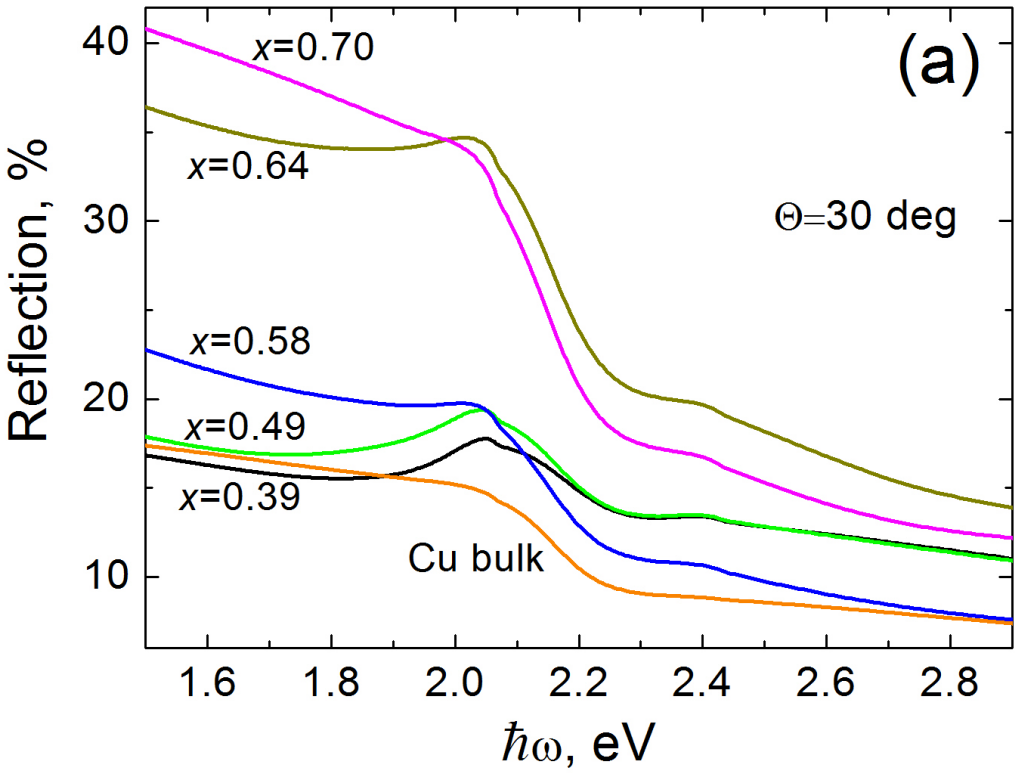
(a)
x=0.70
x=0.64
x=0.58
x=0.49
x=0.39
Cu bulk
Θ=30 deg
Reflection, %
ħω, eV
40
30
20
10
1.6
1.8
2.0
2.2
2.4
2.6
2.8

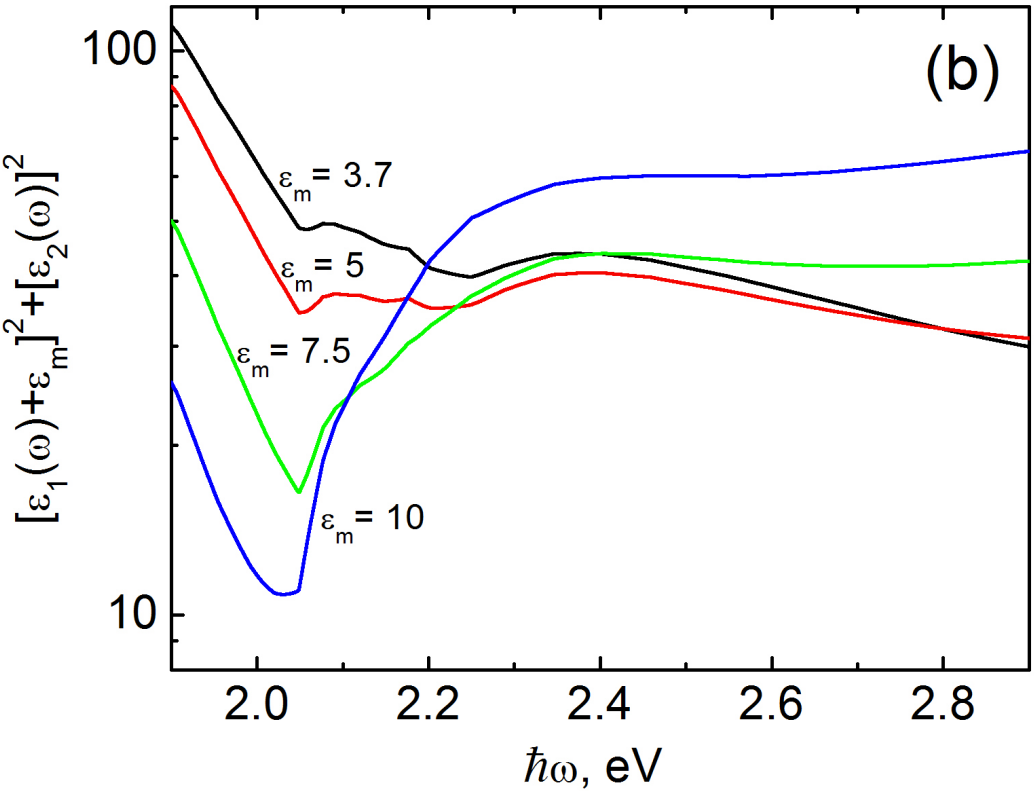
100
10
(b)
ε_m = 3.7
ε_m = 5
ε_m = 7.5
ε_m = 10
$[\varepsilon_1(\omega)+\varepsilon_m]^2+[\varepsilon_2(\omega)]^2$
2.0
2.2
2.4
2.6
2.8
$\hbar\omega$, eV

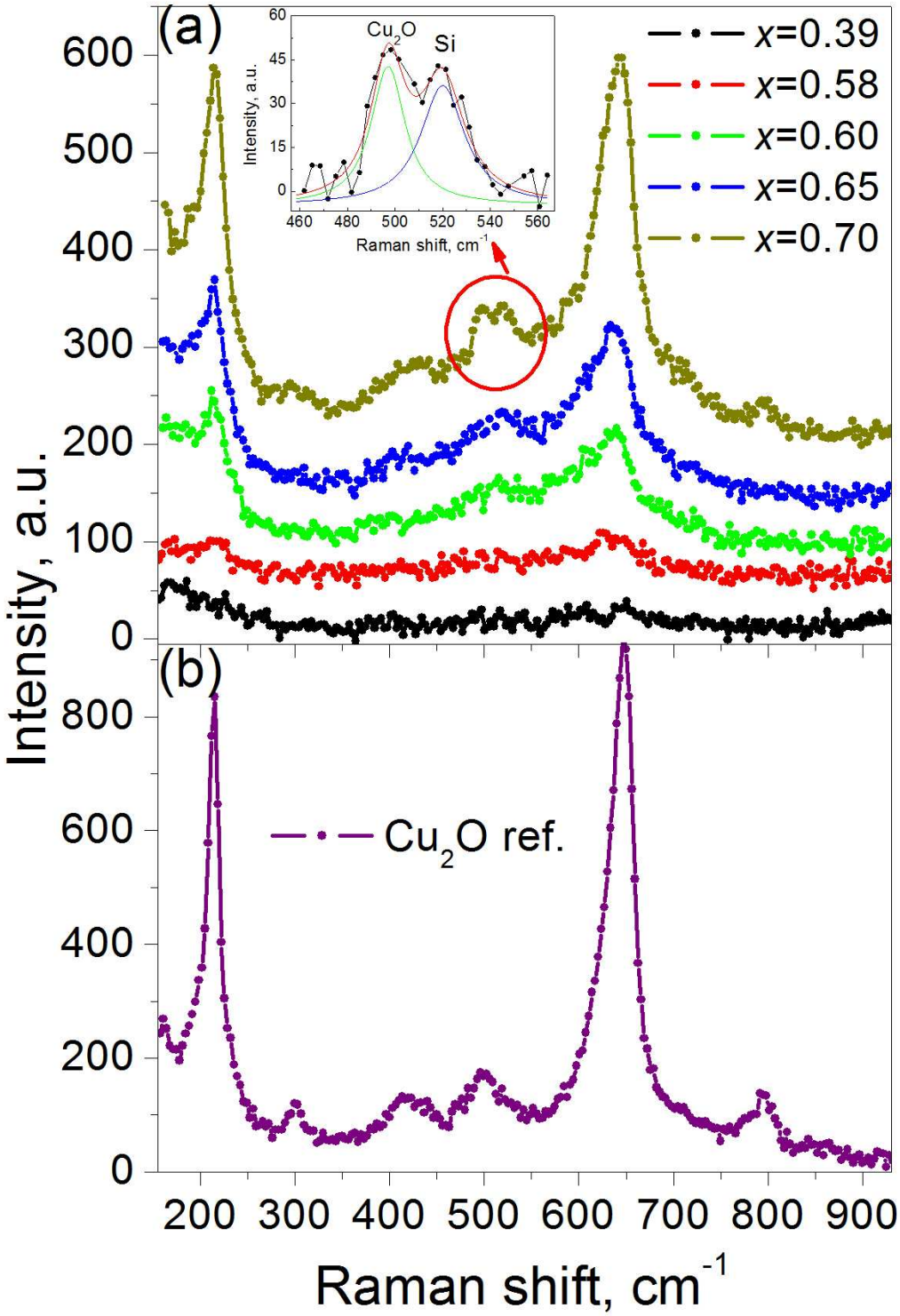
(a)
(b)
x=0.39
x=0.58
x=0.60
x=0.65
x=0.70
Cu2O ref.
Cu2O
Si
Intensity, a.u.
Raman shift, cm-1

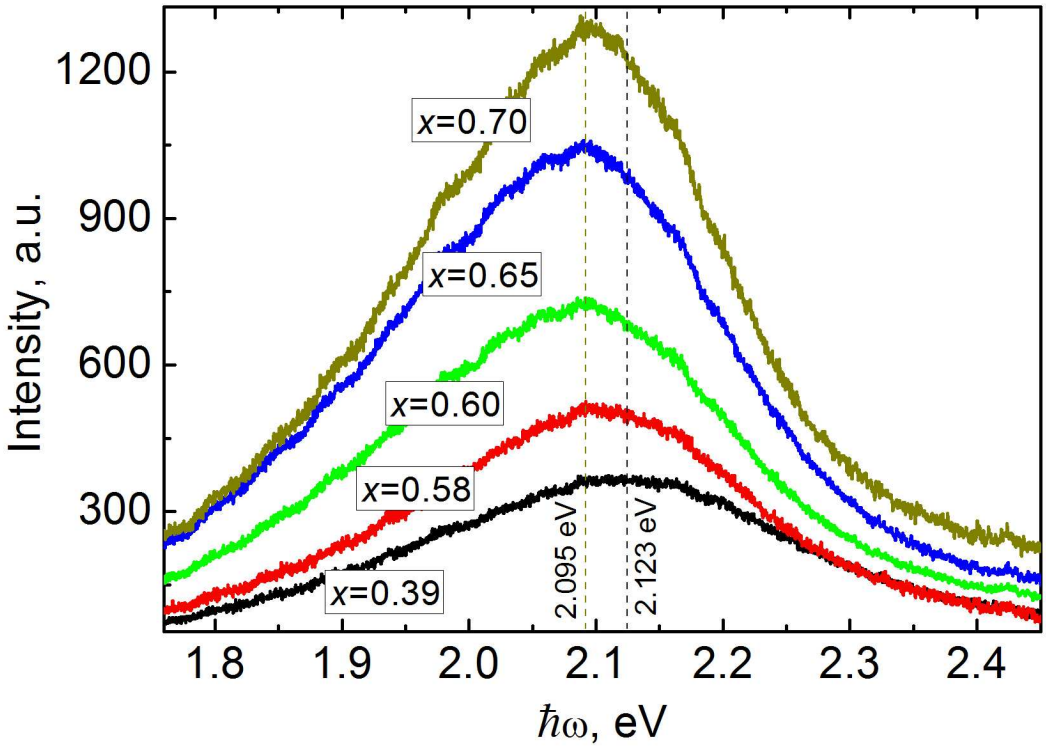

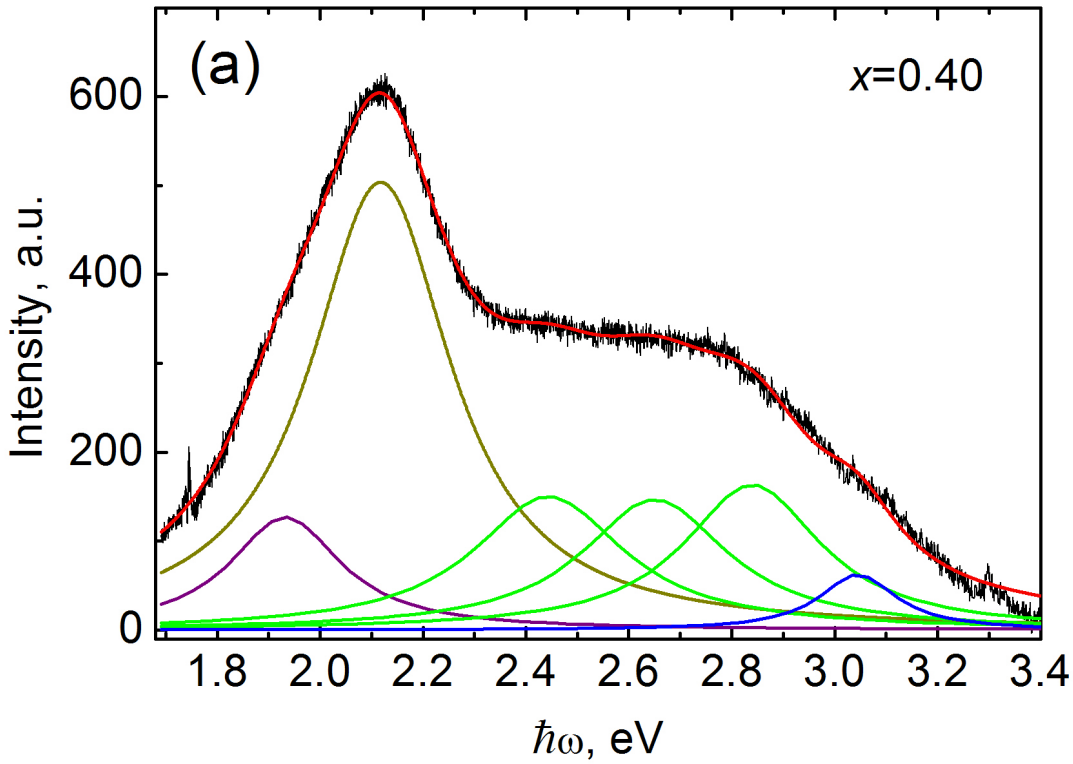

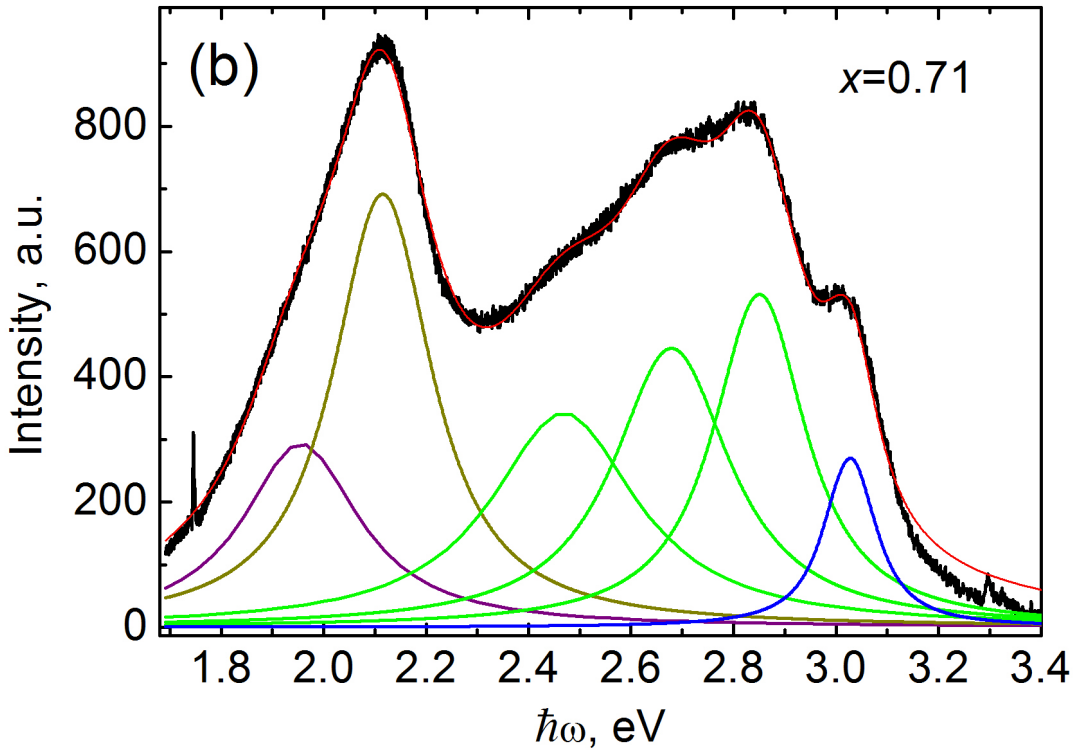

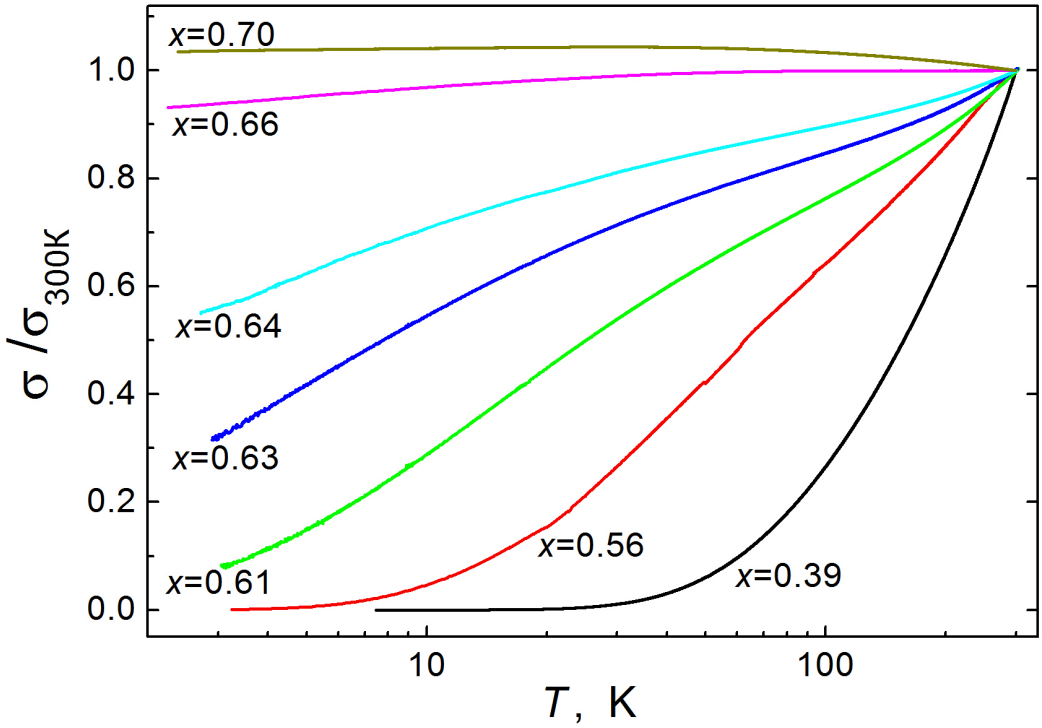

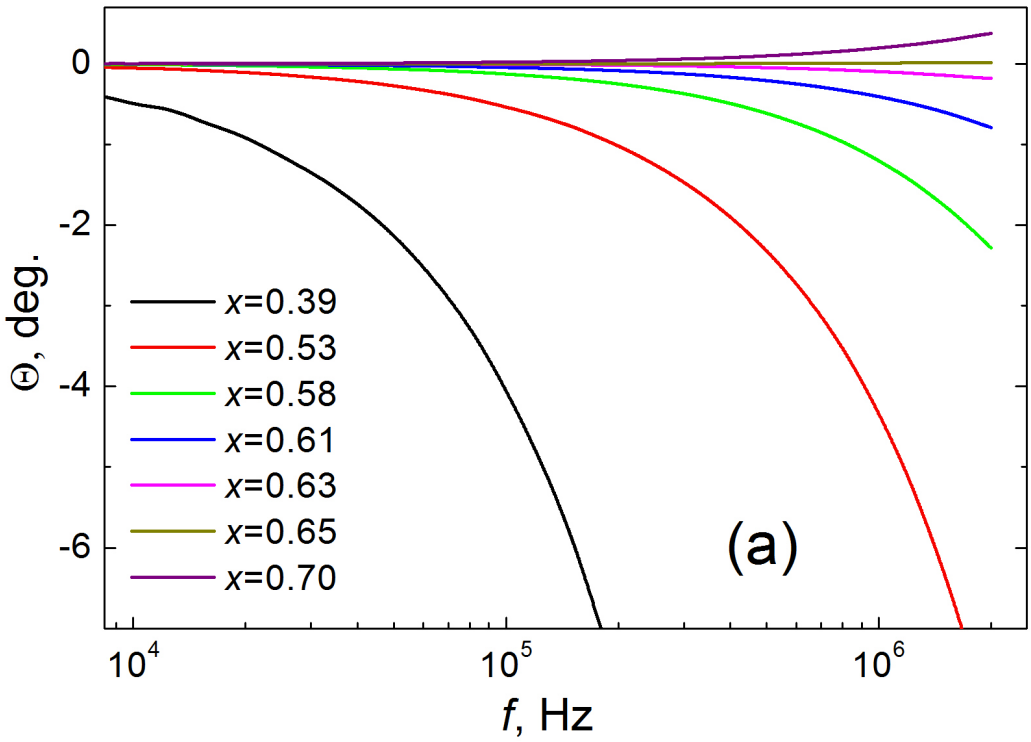

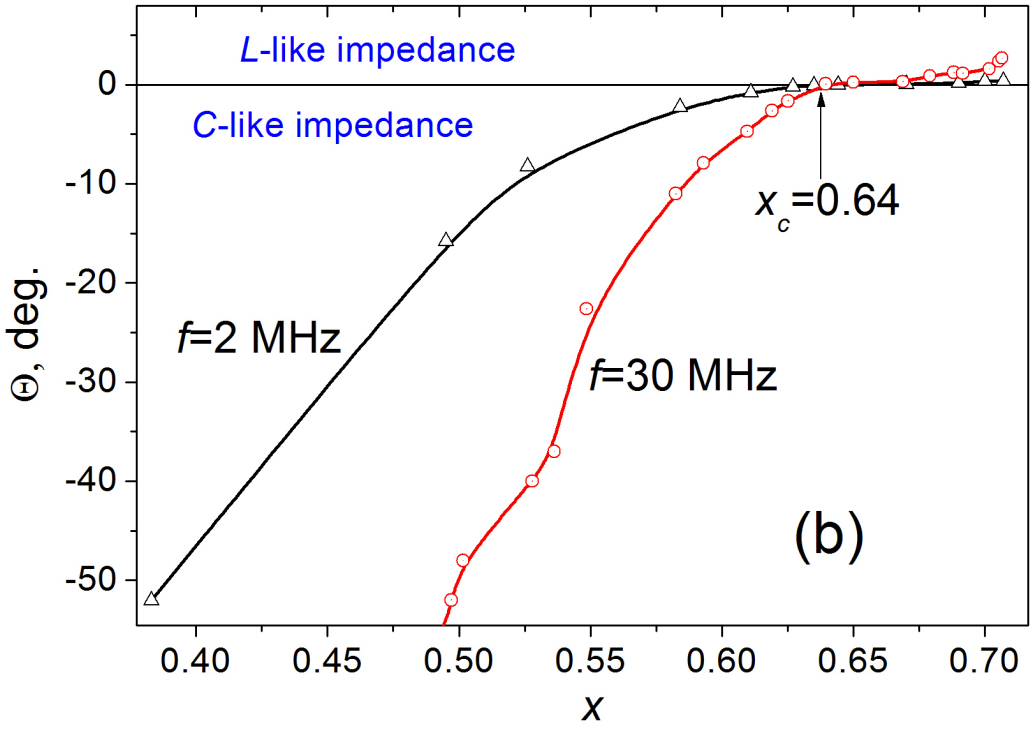

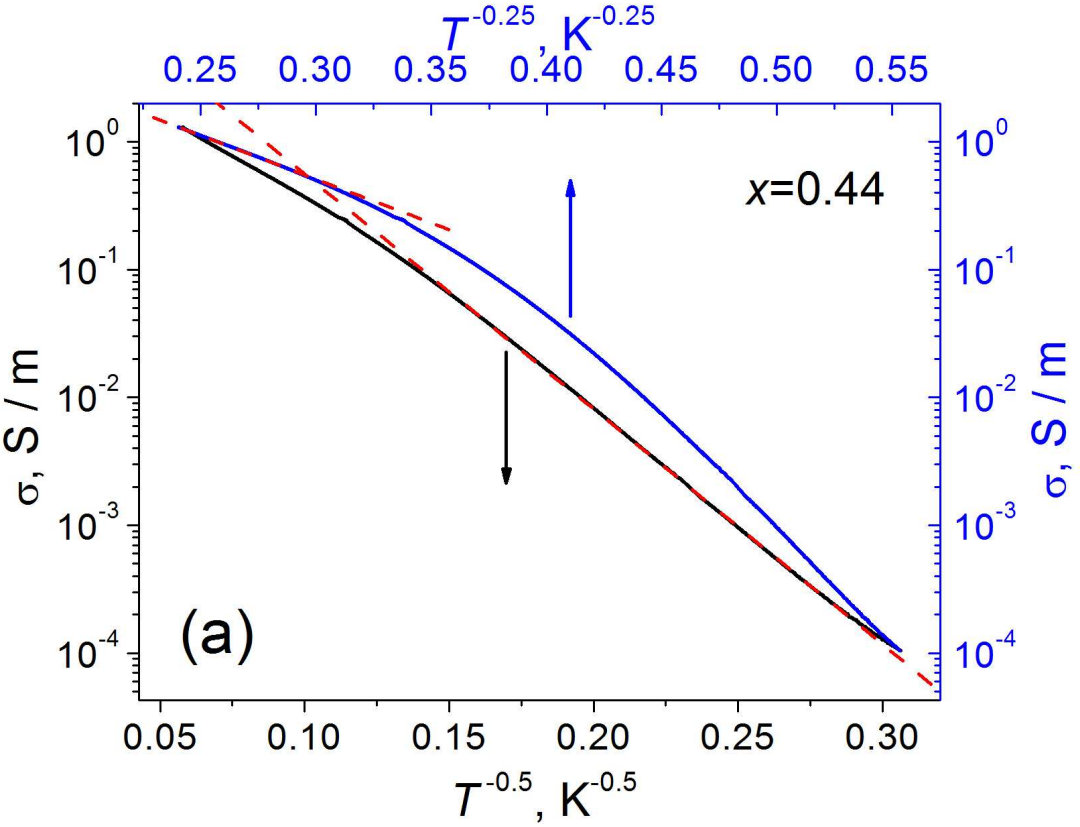

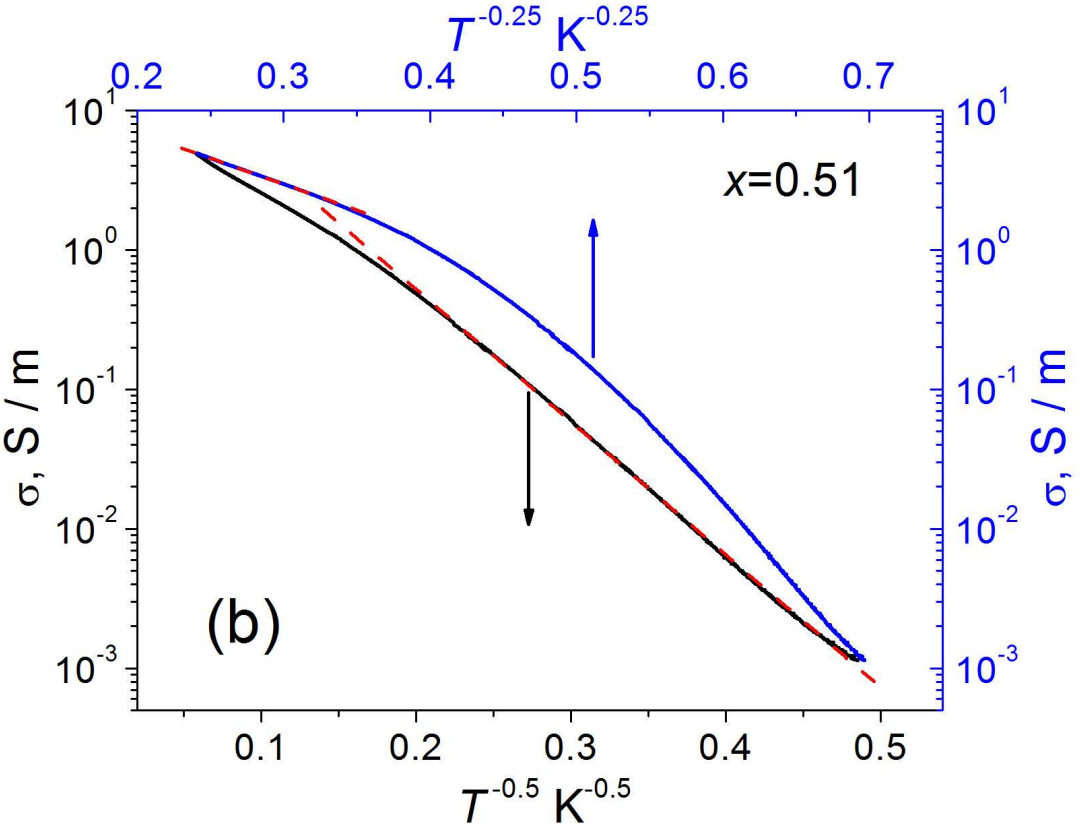

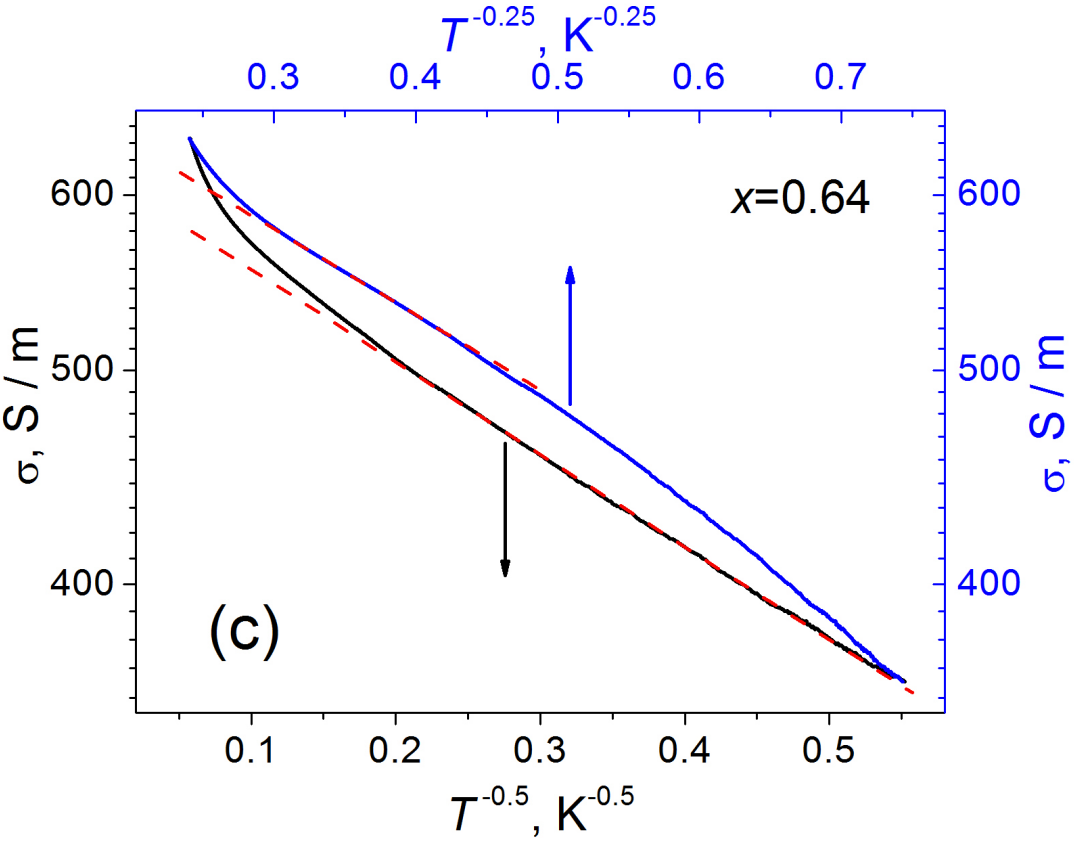

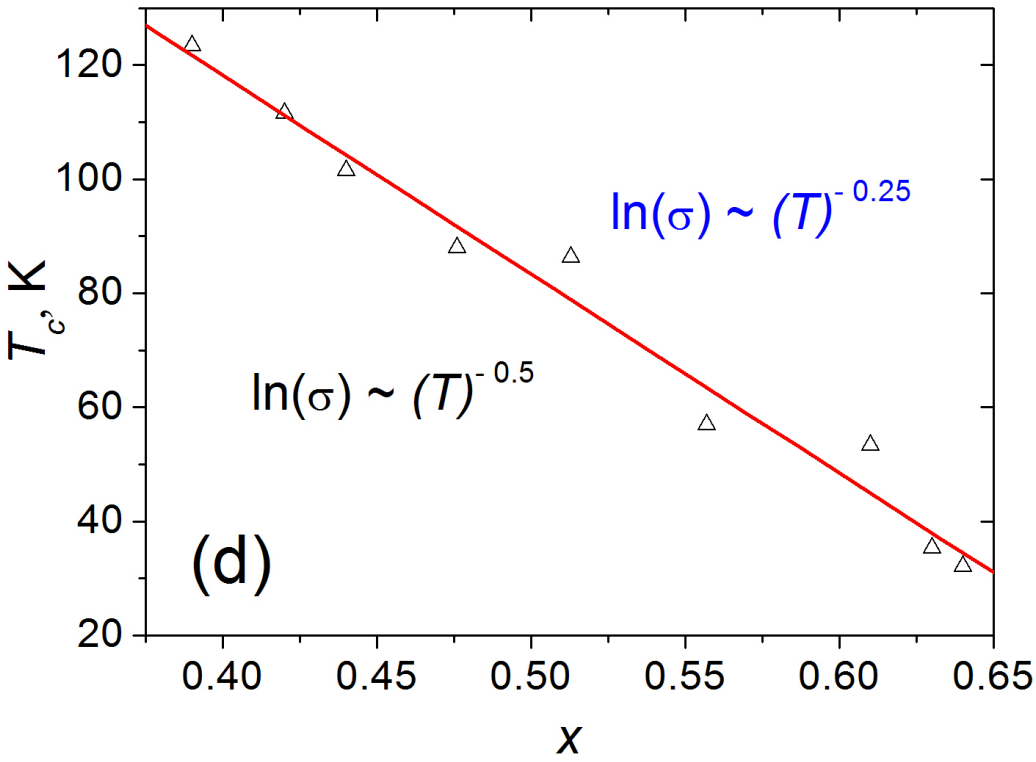
120
100
80
60
40
20
T_c, K
0.40
0.45
0.50
0.55
0.60
0.65
x
ln(σ) ~ $(T)^{-0.25}$
ln(σ) ~ $(T)^{-0.5}$
(d)

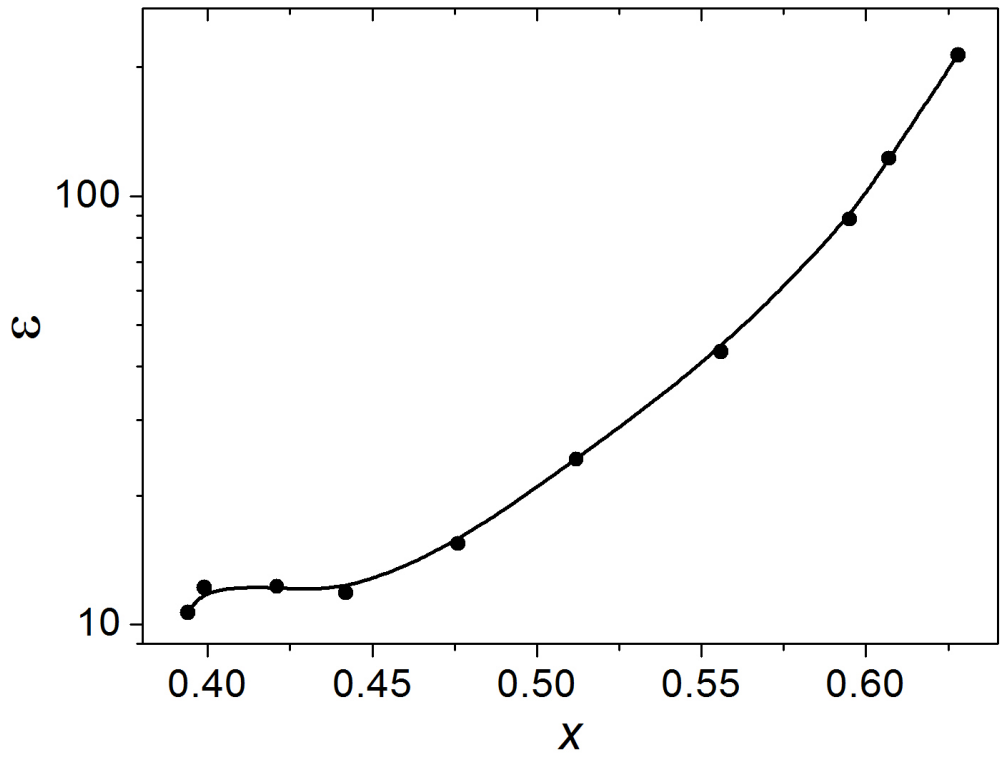

Copper-silicon dioxide nanocomposites: structure and electron transport

Nanostructured composites were prepared by ion-beam sputtering of Cu + SiO_2 target

Increasing copper content leads to progressive formation of defects in oxide matrix

This allows to control matrix permittivity and electron transport in composites